Effects of resistivity on standing shocks in low angular momentum flows around black holes

Chandra B. Singh[1], Toru Okuda[2] and Ramiz Aktar[3]

[1] South-Western Institute for Astronomy Research, Yunnan University, Kunming 650500, China; *chandrasingh@ynu.edu.cn*

[2] Hakodate Campus, Hokkaido University of Education, Hachiman-Cho 1-2, Hakodate, Hokkaido 040-8567, Japan

[3] Department of Astronomy, Xiamen University, Xiamen 361005, China

Abstract We study two-dimensional low angular momentum flow around a black hole using the resistive magnetohydrodynamic module of PLUTO code. Simulations have been performed for the flows with parameters of specific angular momentum, specific energy and magnetic field which may be expected for the flow around Sgr A*. For flows with lower resistivity $\eta = 10^{-6}$ and 0.01, the luminosity and shock location on the equator vary quasi-periodically. The power density spectra of luminosity variation show peak frequencies which correspond to the periods of 5×10^5, 1.4×10^5 and 5×10^4 s. These quasi-periodic oscillations (QPOs) occur due to interaction between the outer oscillating standing shock and the inner weak shocks occurring at the innermost hot blob. While for cases with higher resistivity $\eta = 0.1$ and 1.0, the high resistivity considerably suppresses the magnetic activity such as MHD turbulence and the flows tend to be steady and symmetric with respect to the equator. The steady standing shock is formed more outward compared with the hydrodynamical flow. The low angular momentum flow model with the above flow parameters and with low resistivity has a possibility to explain long-term flares of Sgr A* with frequencies $\sim$ one per day and $\sim 5 - 10$ days in the latest observations by Chandra, Swift and XMM-Newton monitoring of Sgr A*.

Key words: accretion, accretion disks — magnetohydrodynamics (MHD) — methods: numerical — shock waves — Galaxy: center

1 INTRODUCTION

Black hole accretion is the most efficient process which can address the issue of power generated in the neighborhood of a black hole. Historically, the study of black hole accretion has been based on two extreme cases of accretion process: radiatively inefficient flow called Bondi flow (Bondi 1952; Michel 1972) and radiatively efficient one called Keplerian disk (Shakura & Sunyaev 1973; Novikov & Thorne 1973). Both suffer from certain limitations. Spherical Bondi flow with zero angular momentum is quite fast but cannot explain the high luminosities associated with observational signatures around the black hole. However, in reality, accretion flow is supposed to have some amount of angular momentum associated with it. On the other hand, a cold, thin, Keplerian disk cannot explain the issue of change in spectral states and associated

temporal variabilities and it is not applicable for the close region around the black hole as pressure gradient and advective radial velocity terms are ignored.

Accretion flow onto the black hole is supposed to be supersonic at the event horizon and subsonic at a large distance as the accretion flow approaches the speed of light at the horizon with sound speed being of lesser value. So, the flow with angular momentum must pass through at least one sonic point before plunging onto the black hole and should be advective (Liang & Thompson 1980). In case of accretion onto a star, even a small angular momentum will stop the matter fall onto its surface because of the infinite potential barrier associated with the Newtonian potential. Whereas in the case of a black hole, gravity always wins over centrifugal force because of higher-order terms (Chakrabarti 1993). Not only that, for given values of specific energy and specific angular

momentum of accretion flow around the black hole, multiple sonic points may also exist with the possibility of standing shocks (Fukue 1987; Chakrabarti 1989). There have been several interesting works which explored the solutions with standing shocks in pseudo-Newtonian potential (Paczyńsky & Wiita 1980) taking into account various prescriptions for alpha parameter (Chakrabarti 1996; Becker et al. 2008; Kumar & Chattopadhyay 2013). General relativistic solutions for inviscid (Das et al. 2015) and viscous disks (Chattopadhyay & Kumar 2016) with standing shocks have also been reported. Even in the presence of a magnetic field, formation of standing shocks in accretion flows have been explored (Takahashi et al. 2006; Fukumura et al. 2007).

In recent time the model which has received wide recognition is the advection dominated accretion flow (ADAF) (Narayan & Yi 1994; Narayan et al. 1997) solution which takes care of the inner boundary condition around the black hole, however it has only one sonic point close to the black hole. It should be noted that advective flow with multiple sonic points may not necessarily be ADAF-type especially when a standing shock exists in the accretion flow (Chakrabarti 1996). Overall, ADAF solutions occupy a small region of parameter space for given specific energy and specific angular momentum (Lu et al. 1999; Kumar & Chattopadhyay 2013, 2014). The need for a sub-Keplerian component was presented in addition to the Keplerian one. The sub-Keplerian component can undergo shock transition and form a hot, puffed up region like a corona (Chakrabarti & Titarchuk 1995). The properties of a post-shock region formed from the natural course of flow dynamics can address issues like state transitions (Mandal & Chakrabarti 2010), origin of hard power-tail and low frequency quasi-periodic oscillations (QPOs) (Chakrabarti et al. 2015) and also the origin of outflows (Das et al. 2001; Singh & Chakrabarti 2011; Aktar et al. 2015).

In the last 25 years, there have been a significant amount of simulation works dedicated to exploring the formation of a standing shock in low angular momentum sub-Keplerian advective flows around black holes. Using smoothed particle hydrodynamics (SPH) simulations, stable standing shocks were shown to form in one-dimensional (Chakrabarti & Molteni 1993) and two-dimensional setups (2D) (Molteni et al. 1994) as predicted by semi-analytical solutions of inviscid flows (Chakrabarti 1989). For the first time, the dependence of standing shock stability on values of viscosity parameters was confirmed by SPH simulations as well (Chakrabarti & Molteni 1995). The origin of outflows from the post-shock region in accretion disks was verified in simulations incorporat-

ing SPH (Molteni et al. 1996), Eulerian total variation diminishing (TVD) (Ryu et al. 1997; Okuda et al. 2007) and Lagrangian TVD (Lee et al. 2016). In the presence of cooling, the post-shock region may oscillate as the cooling time scale becomes comparable to free-fall time scale and can be responsible for QPOs in case of stellar mass as well as supermassive black holes (Molteni et al. 1996; Okuda et al. 2007). Besides the case of inviscid flow, viscosity can also induce shock oscillations and give rise to QPOs (Lanzafame et al. 1998; Chakrabarti et al. 2004; Lanzafame et al. 2008; Lee et al. 2011; Das et al. 2014; Lee et al. 2016). There have been some works regarding stability or instability of the shock and shocks seem to be stable against axisymmetric (Nakayama 1992, 1994; Nobuta & Hanawa 1994; Le et al. 2016) as well as non-axisymmetric perturbations (Molteni et al. 1999; Gu & Foglizzo 2003; Gu & Lu 2006). Recently it has been established through numerical simulations that advective flow can be segregated into two components, Keplerian as well as sub-Keplerian, in the presence of viscous heating and cooling processes (Giri & Chakrabarti 2013; Giri et al. 2015; Roy & Chakrabarti 2017). All the above-mentioned simulation works addressed the accretion flow behavior around a non-rotating black hole by relying on pseudo-Newtonian potential. Recently, general relativistic high-resolution shock-capturing simulation code was used to study the scenario in Schwarzschild (Kim et al. 2017) and Kerr (Kim et al. 2019) space-time which further established the formation of a standing shock in hydrodynamic (HD) flow around a non-rotating as well as rotating black hole in full general relativistic treatment. However, till now there has been only one work taking into account different magnitudes of magnetic field strength in such flows in the presence of standing shocks (Okuda et al. 2019). The long term evolution properties were investigated and long term flares in connection with Sgr A⋆ could be explained.

Simulation works dealing with advective flows usually take into account two types of setup: torus equilibrium solution (e.g., Stone & Pringle 2001; McKinney & Gammie 2002) and Bondi flow along with arbitrary choice of specific angular momentum (Proga & Begelman 2003). Our study involves a third and different kind of set up where we take initial conditions based on exact solutions of HD equations (Chakrabarti 1989). We are dealing with a big gap in parameter space which lies between the regime of high angular momentum torus and zero angular momentum Bondi flow. To make our study simpler, we are dealing with inviscid flows having constant and small specific angular momentum value which are lower than that of Keplerian value of the specific angular momentum for an innermost stable circular orbit. Such low angular

momentum flows are likely to be present in black hole X-ray binary systems accreting winds from a companion star as well as in active galactic nuclei where winds from stellar clusters collide and lose angular momentum before getting accreted onto the central black holes (Chakrabarti & Titarchuk 1995; Smith et al. 2001, 2002; Moscibrodzka et al. 2006). The objective of our work is to study the effects of resistivity with varying magnitude on the formation and stability of standing shocks in low angular momentum accretion flows around the black holes, which have not been explored before.

Section 2 shows details of 1.5 dimensional (1.5D) theoretical solutions which have been used for the simulation set up. In Section 3, basic equations solved by simulation code are presented. Besides, the details of computational domain, and initial and boundary conditions are described in Section 3. Section 4 contains details of numerical results followed by Section 5 where we present a summary and discussion of our work.

2 THEORETICAL SOLUTION

We consider a semi-analytical approach for solving the standard conservation equations under HD framework. The calculations are done in cylindrical coordinates with coordinates R and z. Axisymmetry is assumed for the angular ϕ coordinate. For simplicity, we further assume that the flow velocity along the vertical direction is zero and therefore only integrate along the radial coordinate assuming vertically averaged dynamical quantities.

We define the scale radius as Schwarzschild radius $r_g = 2GM/c^2$, with M being the mass of the central compact object, G the gravitational constant and c is the speed of light. The matter that is accreted onto the central compact object has radial velocity given by u_R, specific angular momentum L and total specific energy $\mathcal{E}$. As the semi-analytical calculations are carried out with non-dimensional quantities, we define the following

$$r = \frac{R}{r_g}; \; h = \frac{z}{r_g}; \; v_R = \frac{u_R}{c}; \; \lambda = \frac{L}{r_g c}; \; \epsilon = \frac{\mathcal{E}}{c^2}. \quad (1)$$

For studying an ideal, inviscid flow onto a compact object, we deal with the mass conservation equation,

$$\dot{M} = 4\pi \rho v_R r h, \quad (2)$$

where ρ is the density and h is the half-thickness of the flow. Energy conservation gives us a relation of specific energy of the flow or Bernoulli constant,

$$\epsilon = \frac{v_R^2}{2} + \frac{c_s^2}{\Gamma - 1} + \frac{\lambda^2}{2r^2} + \Phi. \quad (3)$$
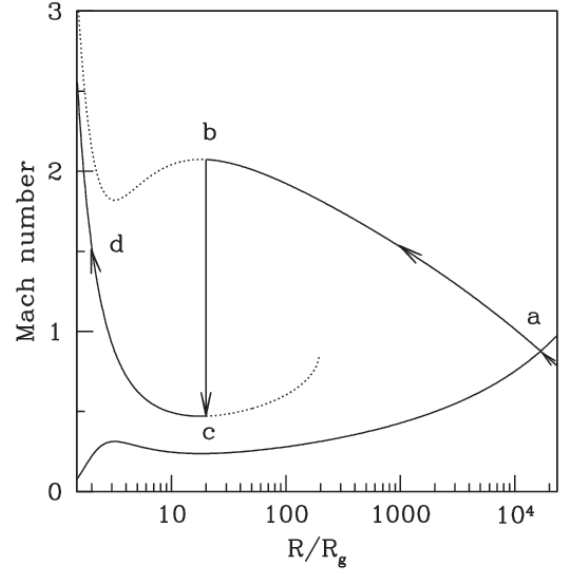

Fig. 1 Mach number versus radial distance from semi-analytical estimates for flow parameters, specific energy, $\epsilon = 1.98 \times 10^{-6}$ and specific angular momentum, $\lambda = 1.35$, with $\Gamma = 1.6$ (adopted from Okuda et al. 2019).

Here c_s is adiabatic sound speed in units of c and Γ is the adiabatic index. $c_s = \sqrt{\frac{\Gamma p}{\rho c^2}}$. p is the thermal pressure and Φ is the non-dimensional gravitational potential given by $-1/2(x-1)$ for a non-rotating black hole (Paczyńsky & Wiita 1980) where $x = r_{sp}/r_g$ and r_{sp} is the spherical radius. Considering the vertical equilibrium condition, we evaluate the radial dependence for h

$$h = c_s \sqrt{x}(x-1). \quad (4)$$

For given values of ϵ and λ, we solve Equations (2) and (3) and look for transonic conditions. Differentiating Equations (2) and (3), we obtain

$$\frac{dv_R}{dr}\left[v_R - \frac{2c_s^2}{(\Gamma+1)v_R}\right] = \frac{2c_s^2}{\Gamma+1}\frac{d\ln f}{dr} - \frac{dG}{dr}, \quad (5)$$

where $G = \lambda^2/2r^2 - 1/2(r-1)$ and $f = 2r^{3/2}(r-1)$ (Chakrabarti 1989). At critical points, the vanishing left-hand side gives radial velocity,

$$(v_R)_{crit} = \sqrt{\frac{2}{\Gamma+1}}(c_s)_{crit}, \quad (6)$$

and the vanishing right hand side yields sound speed

$$(c_s)_{crit} = \frac{(\Gamma+1)(r_{crit}-2)}{r_{crit}^2}\frac{(\lambda_K^2 - \lambda^2)}{(5r_{crit}-2)}. \quad (7)$$

The subscript $crit$ and K represent quantities at the critical points and Keplerian orbits respectively. In the case we obtain multiple critical points, we also check whether

shock conditions are satisfied or not along the accretion flow. If shock conditions are satisfied, then there is a possibility of standing axisymmetric shock, otherwise not. The shock location can be determined using an invariant quantity, C, across the shock which is given by

$$
\begin{aligned}
C &= \frac{[\mathcal{M}_+(3\Gamma - 1) + (2/\mathcal{M}_+)]^2}{2 + (\Gamma - 1)\mathcal{M}_+^2} \\
&= \frac{[\mathcal{M}_-(3\Gamma - 1) + (2/\mathcal{M}_-)]^2}{2 + (\Gamma - 1)\mathcal{M}_-^2} .
\end{aligned}
\tag{8}
$$

Here, $\mathcal{M} = v_{\mathrm{R}}/c_s$ is the Mach number of the accretion flow. The subscripts $-$ and $+$ represent quantities in the pre-shock and post-shock region respectively. Further details on the semi-analytical approach can be found in Chakrabarti (1989).

Figure 1 plots the variation of Mach number, $\mathcal{M}$, of flow with radial distance from the black hole obtained from exact theoretical solution solving conservation equations. The transonic flow passes through the outer critical point "a" and continues its journey towards the black hole. The flow chooses to undergo shock transition along "bc", becomes subsonic then again accelerates towards the black hole and passes through inner critical point "d" to become supersonic before entering the black hole horizon. The shocked flow is preferable in nature as the entropy generation is relatively higher compared to no shock flow.

3 NUMERICAL SETUP

3.1 Basic Equations

The numerical setup for the present work uses grid-based, finite volume computational fluid dynamics code, PLUTO (Mignone et al. 2007, 2012). Numerical simulations are carried out by solving the equations of classical resistive magnetohydrodynamics (MHD) in the conservative form:

$$
\frac{\partial \rho}{\partial t} + \nabla \cdot (\rho \mathbf{v}) = 0 ,
\tag{9}
$$

$$
\frac{\partial (\rho \mathbf{v})}{\partial t} + \nabla \cdot [\rho \mathbf{v} \mathbf{v} - \mathbf{B} \mathbf{B}] + \nabla p_t = -\rho \nabla \Phi ,
\tag{10}
$$

$$
\frac{\partial E}{\partial t} + \nabla \cdot [(E + p_t)\mathbf{v} - (\mathbf{v} \cdot \mathbf{B})\mathbf{B} + \eta(\nabla \times \mathbf{B}) \times \mathbf{B}] = -\rho \mathbf{v} \cdot \nabla \Phi ,
\tag{11}
$$

$$
\frac{\partial \mathbf{B}}{\partial t} - \nabla \times (\mathbf{v} \times \mathbf{B} - \eta \nabla \times \mathbf{B}) = 0 .
\tag{12}
$$

Here, p_t is the total pressure with contribution from thermal pressure, p, and magnetic pressure, $B^2/2$. E is the total energy density expressed as

$$
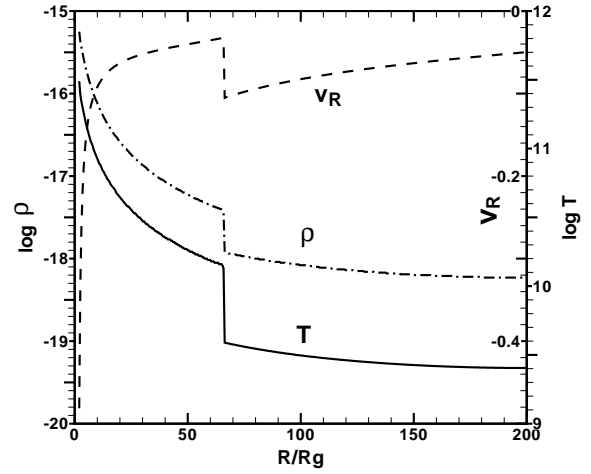E = \frac{p}{\Gamma - 1} + \frac{1}{2}(\rho \mathbf{v}^2 + \mathbf{B}^2) .
\tag{13}
$$

Fig. 2 Flow parameters on the equator, namely density (ρ in $\mathrm{g\,cm^{-3}}$), radial velocity (v_R) and temperature (T), for the final state of the HD simulation run. The standing shock is at $64.8 R_g$ (adapted from Okuda et al. 2019).

η is the resistivity for which a range of values has been chosen, 10^{-6}, 0.01, 0.1 and 1. Vector potential $\mathbf{A}$ is prescribed to generate the magnetic field $\mathbf{B}$ as $\mathbf{B} = \nabla \times \mathbf{A}$. Following Proga & Begelman (2003), the components of $\mathbf{A}$ are as follows: $A_R = 0$, $A_\phi = \frac{A_0 z}{r_{\mathrm{sp}} R}$ and $A_z = 0$. Here, $A_0 = \mathrm{sign}(z)(\frac{8\pi p_{\mathrm{out}}}{\beta_{\mathrm{out}}})^{1/2} R_{\mathrm{out}}^2$ and $\beta_{\mathrm{out}} = 8\pi p_{\mathrm{out}}/B_{\mathrm{out}}^2$, where subscript "out" denotes parameters at the outer boundary of the computational domain, R_{out}. Following Okuda et al. (2019), we take a typical value of 5000 for β_{out}.

3.2 Initial and Boundary Conditions

First, we have studied advective flows onto black holes in axisymmetric 2D cylindrical geometry (R, z) in an HD framework. The theoretical solutions given in Section 2 provide initial conditions of primitive variables, radial and azimuthal velocity components, density and pressure for a 2D HD set up. Once the HD flow with the standing shock achieves a steady state, we use the solutions as the initial conditions for the magnetized flow with resistivity and let the simulation evolve further. The computational domain is $0 \le R \le 200 R_g$ and $-200 R_g \le z \le 200 R_g$ with the resolution of 1640×820 cells (for details, see Okuda et al. 2019). Though we performed some simulation runs at half resolution, 820×410, and double resolution, 3280×1640, the results remain unchanged.

In both HD and MHD runs, the same boundary conditions are imposed. At the outer radial boundary, $R_{\mathrm{out}} = 200 R_g$, there are two domains: the disk region where the matter is injected and the atmosphere above the

disk region. The flow parameters given by 1.5D theoretical solutions are provided in the region $-h_{\text{out}} \leq z \leq h_{\text{out}}$ where h_{out} is the vertical equilibrium height at R_{out}. For the atmosphere region, the matter is allowed to leave the domain but not enter. The axisymmetric boundary condition is implemented at the inner radial boundary. At $R = 2R_g$, the absorbing condition is imposed in the computational domain. In the vertical direction, $z = \pm 200R_g$, standard outflow boundary conditions are imposed. In the case of the MHD run, a constant magnetic field is imposed on the outer radial boundary. Figure 2 shows profiles of density (ρ in g cm^{-3}), radial velocity (v_R) and temperature (T) of the HD flow. The standing shock location from the simulation run is at $\sim 65R_g$ which is significantly different from the predicted location from the theoretical solution, i.e. $\sim 20R_g$. This is due to the assumption of vertical hydrostatic equilibrium applied in the 1.5D transonic solutions, which is valid as long as the disk thickness h is sufficiently small compared with the radius r (that is, $h/r \ll 1$). However, in many cases of low angular momentum flow with standing shock, $h/r \sim 0.1$–0.5 because such flows are intrinsically advective and geometrically thick. Therefore, if the outer radial boundary is chosen to be very far from the predicted theoretical shock location, the difference between the numerical and theoretical shock locations becomes significant (Okuda et al. 2019).

4 RESULTS AND DISCUSSION

To ascertain the characteristic features of the flow, we examine the time evolution of shock location R_s on the equator and total luminosity L of the flow. The luminosity L is calculated as follows, assuming that the gas is optically thin

$$L = \int q_{ff} dV , \qquad (14)$$

where q_{ff} represents the free-free emission rate per unit volume and integration is performed over the whole computational domain. In order to have some estimate of how much matter is lost as an outflow from the system, mass outflow rate in the z-direction is expressed as,

$$\dot{M}_{\text{out}} = \int_0^{R_{\text{out}}} 2\pi\rho(R, z_{\text{out}})v_z(R, z_{\text{out}})RdR$$
$$- \int_0^{R_{\text{out}}} 2\pi\rho(R, -z_{\text{out}})v_z(R, -z_{\text{out}})RdR, \qquad (15)$$

where v_z is the vertical velocity.

In the present study, the time variability of the flow will correlate with the magnetorotational instability (MRI). We check whether the flow is subject to the MRI and

whether we can resolve the fastest growing MRI mode or not. The stringent diagnostics of spatial resolution for MRI have been examined in three-dimensional magnetized flow. Therefore, its application to our 2D magnetized flow may be limited. The critical wavelength of the instability mode is given by $\lambda_{\text{c}} = 2\pi v_{\text{A}}/\sqrt{3}\Omega$, where v_{A} and Ω are the Alfvén velocity and angular velocity respectively (Hawley & Balbus 1991; Balbus & Hawley 1998). A criterion value Q_{x} of the MRI resolution is defined by

$$Q_{\text{x}} = \frac{\lambda_{\text{c}}}{\Delta x} , \qquad (16)$$

where Δx is the mesh sizes ΔR and Δz in the radial and vertical directions, respectively. When $Q_{\text{x}} \gg 1$, the flow is unstable against MRI, otherwise, the flow is stable. Figure 3 features 2D contours of radial MRI-criterion Q_r for cases of $\eta = 10^{-6}$ and 1.0 at times $t= 7 \times 10^6$ and 8.7×10^6 s, respectively. The analyses affirm $Q_r \gg 1$ in most regions for both cases. So, both flows are unstable to the MRI. The contours are asymmetric with respect to the equator in the former but symmetric in the latter.

4.1 Luminosity, Shock Location and Mass In/Outflow Rates

Figure 4 depicts how luminosity L and shock location R_s vary with time for different levels of resistivity in the flow. For lower values of resistivity, $\eta = 10^{-6}$ and 0.01, there are features of irregular oscillation in the luminosity L and the standing shock location R_s. As the shock moves towards the black hole, there is an increase in luminosity while the luminosity decreases when the shock recedes away. The shock and luminosity oscillate irregularly with time scales of $\sim 10^5 - 10^6$ s, and the luminosity varies maximumly by a factor of ten around the average L, which is $\sim 3.0 \times 10^{34}$ erg s^{-1}. On the other hand, for relatively high resistivity, 0.1 and 1.0, the oscillatory nature disappears and L and R_s exhibit small modulations or almost steady value at later times. The highly resistive flows behave qualitatively similar to that of HD flow.

The mass inflow $\dot{M}_{\text{edge}}$ and outflow $\dot{M}_{\text{out}}$ rates are presented in Figure 5 corresponding to Figure 4. Similar to our previous work Okuda et al. (2019), it has been established that there is a correlation between L and $\dot{M}_{\text{edge}}$ and between R_s and $\dot{M}_{\text{out}}$. However, the variation of L seems to be opposite in terms of behavior compared to R_s. That means when the post-shock region shrinks, the emission increases, and vice versa. Since the low angular momentum flows are very advective, most of the input gas $\dot{M}_{\text{input}}$ ($\sim 3 \times 10^{20}$ g s^{-1}) falls into the event horizon and $\dot{M}_{\text{edge}}$ is comparable to $\dot{M}_{\text{input}}$ in all cases. However, the mass outflow rate $\dot{M}_{\text{out}}$ in the low resistivity case is
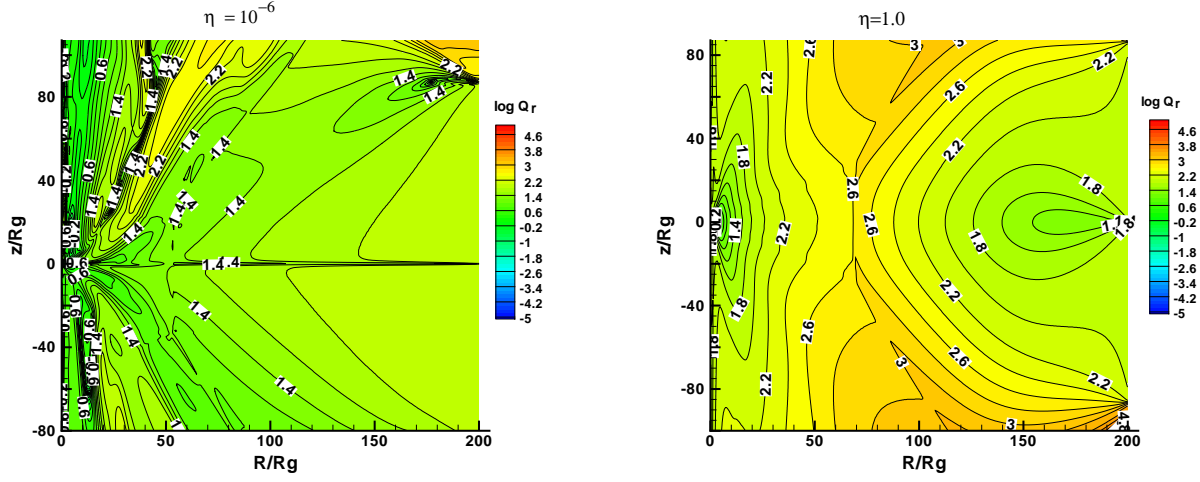
Fig. 3 2D contours of MRI-criterion Q_r for cases of $\eta = 10^{-6}$ and 1.0 at times $t = 7 \times 10^6$ and 8.7×10^6 s, respectively. For both cases, $Q_r \gg 1$ in most regions. The contours are asymmetric with respect to the equator in the former but symmetric in the latter.
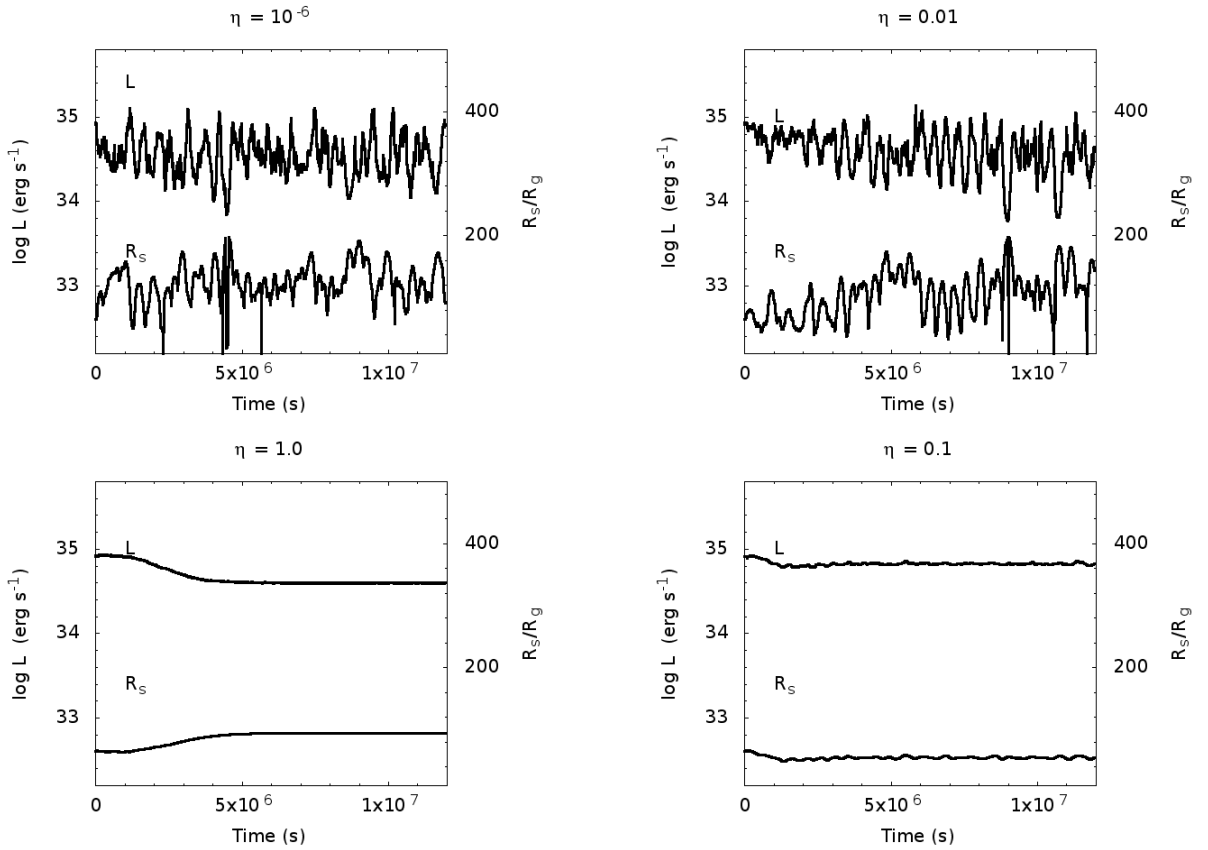

Fig. 4 Variation of luminosity (L) and shock location (R_s) with time for resistive MHD flow with different values of resistivity $\eta = 10^{-6}$, 0.01, 0.1 and 1 (in the clockwise direction).

considerably high at a few tens of percent of the input accretion rate, but in the highly resistive case with $\eta = 0.1$ and 1.0, $\dot{M}_{\mathrm{out}}$ amounts to ~ 10 percent. Such mass outflow rates are very high compared with the mass outflow rate found in the usual accretion flow. It should be noted that the very high mass outflow rate in the low resistivity case may be correlated to the MRI turbulence, that is, the MRI turbulence plays important roles not only in the outward
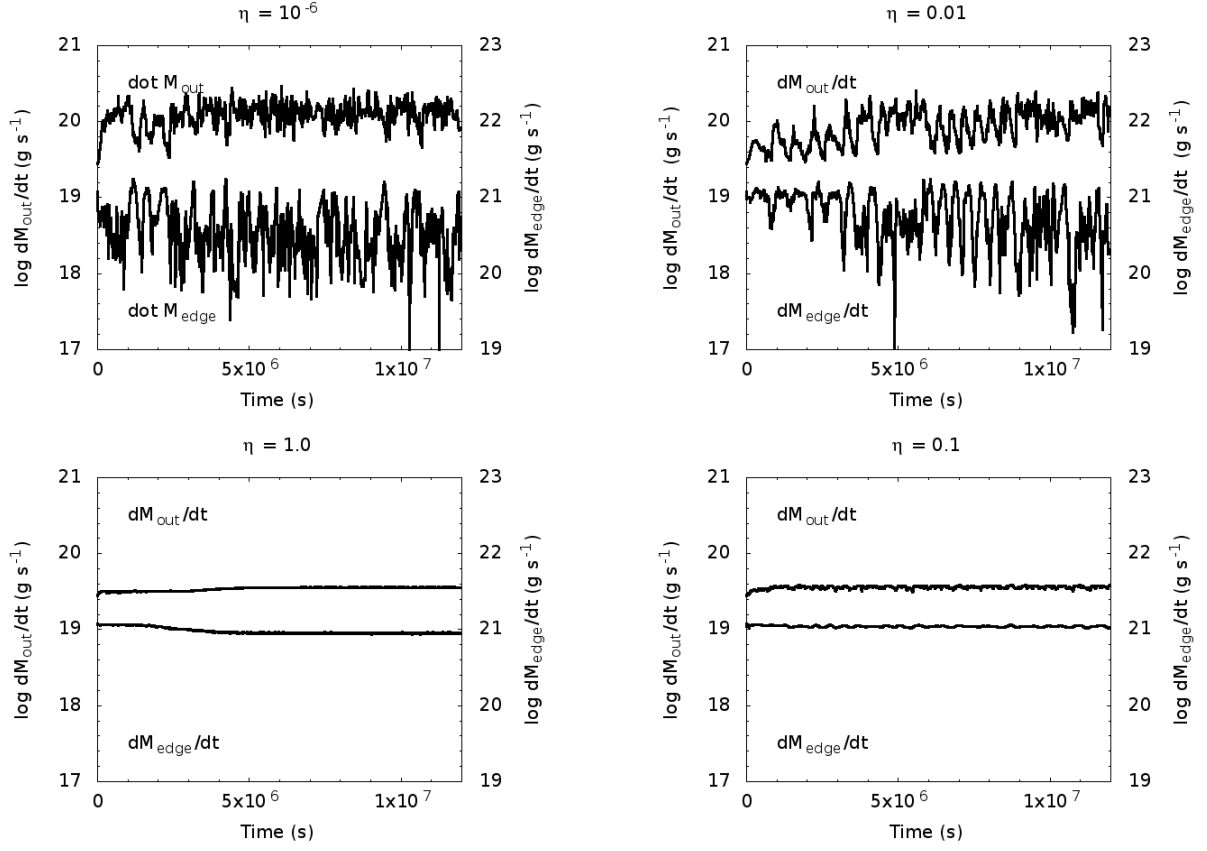
Fig. 5 Mass inflow ($\dot{M}_{\text{edge}}$) as well as outflow ($\dot{M}_{\text{out}}$) rate evolving with time for resistive MHD flow with different values of resistivity $\eta = 10^{-6}$, 0.01, 0.1 and 1 (in the clockwise direction).
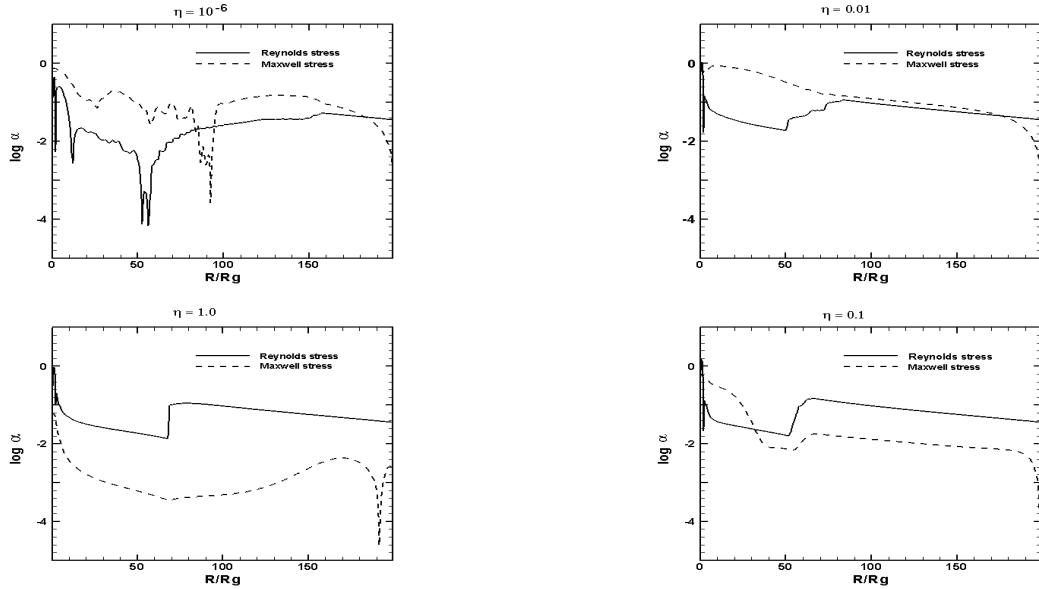

Fig. 6 Radial profiles of normalized Reynolds stress α_{gas} and normalized Maxwell stress α_{mag} for resistive MHD flow with different resistivity $\eta = 10^{-6}$, 0.01, 0.1 and 1 (in the clockwise direction). These values are space-averaged (between $-2R_g$ and $2R_g$ in the z-direction) and time averaged (between 1.1×10^7 and 1.2×10^7 s).
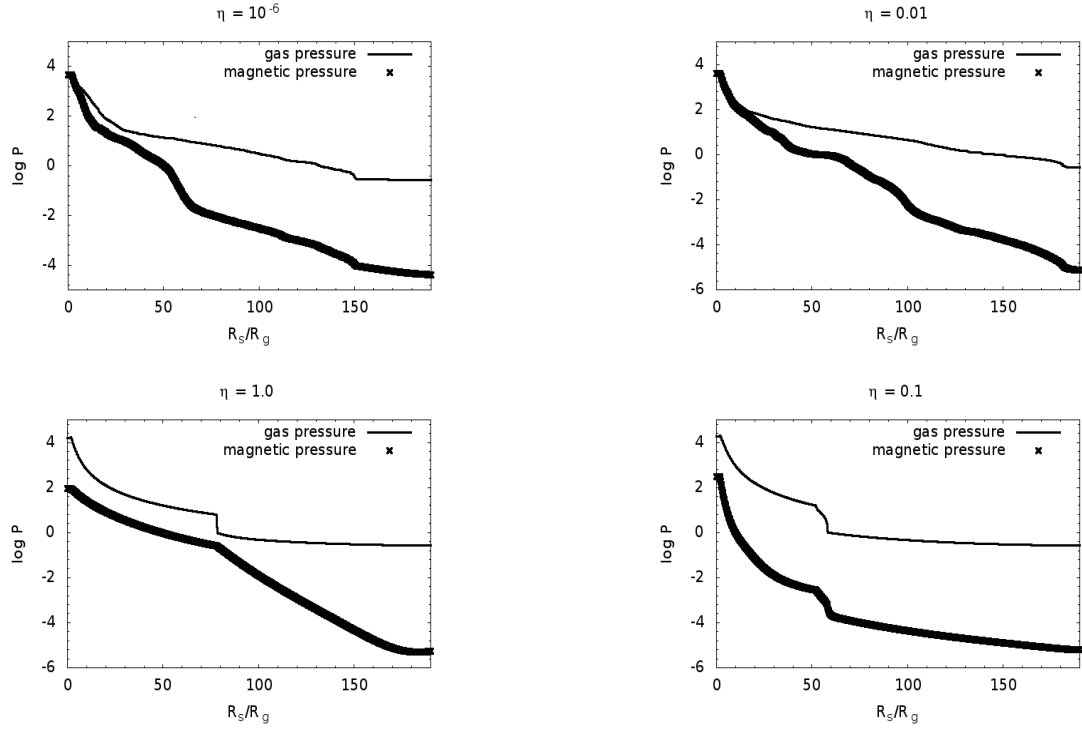
Fig. 7 Radial profiles of gas pressure and magnetic pressure which are space-averaged (between $-2R_g$ and $2R_g$ in the z-direction) and time averaged (between 1.1×10^7 and 1.2×10^7 s) for resistive MHD flow with different resistivity $\eta = 10^{-6}$, 0.01, 0.1 and 1 (in the clockwise direction).

transfer of angular momentum but also in outward mass transfer.

4.2 Effects of Resistivity on Magnetized Flow

The resistivity has dissipative and diffusive characteristics in the magnetic field through the current density, similar to the viscosity in hydrodynamical flow and we expect the higher resistivity to suppress magnetic activity like magnetic turbulence. We examine the effects of resistivity through the time evolution of the magnetized flows with $\eta = 10^{-6}$ to 1.0. In the case with the lowest resistivity 10^{-6}, after a transient initial time evolution, the magnetic field is amplified rapidly by the MRI and MHD turbulence develops near the equatorial plane. Figure 6 displays radial profiles of normalized Reynolds stress α_{gas} and normalized Maxwell stress α_{mag} for resistive MHD flow with different resistivity $\eta = 10^{-6}$, 0.01, 0.1 and 1 (in the clockwise direction). These values are space-averaged (between $-2R_g$ and $2R_g$ in the z-direction) and time averaged over the last duration time. Here we see that the Maxwell stress Σ_{mag} is larger by a factor of a few to ten than the Reynolds stress Σ_{gas} in cases of lower $\eta = 10^{-6}$ and 0.01 over most of the region, while with higher η the Reynolds stress mostly dominates over the

Maxwell stress. From this, we confirm that the higher resistivity suppresses the Maxwell stress and then MHD turbulence, that is, hydrodynamical mode dominates over magnetohydrodynamical mode. As a result, in the case with the highest resistivity, the flow is dominated by hydrodynamical quantities at the outer radial boundary which are symmetric with respect to the equator and the flow achieves a steady and symmetric state. Figure 7 plots radial profiles of the gas pressure and the magnetic pressure for MHD flow with resistivity $\eta = 10^{-6}$, 0.01, 0.1 and 1 (in the clockwise direction). In all cases with different resistivity, the gas pressure dominates the magnetic pressure and the pressure distributions are not so different from each other.

Figure 8 displays 2D density contours and velocity vectors at the later evolution of the flow with $\eta = 10^{-6}$ and 1.0 at times $t = 7 \times 10^6$ and 8.7×10^6 s respectively. Here, the location of the standing shock is distinguished as the thick black contour lines, and the velocity vectors are taken to be an arbitrary unit. In the low resistivity case, the density contours are asymmetric with respect to the equator and turbulent motions are observed in the shocked region. While in the high resistivity case, variables become symmetric with respect to the equator and no turbulent motion is observed. The flow features seem to
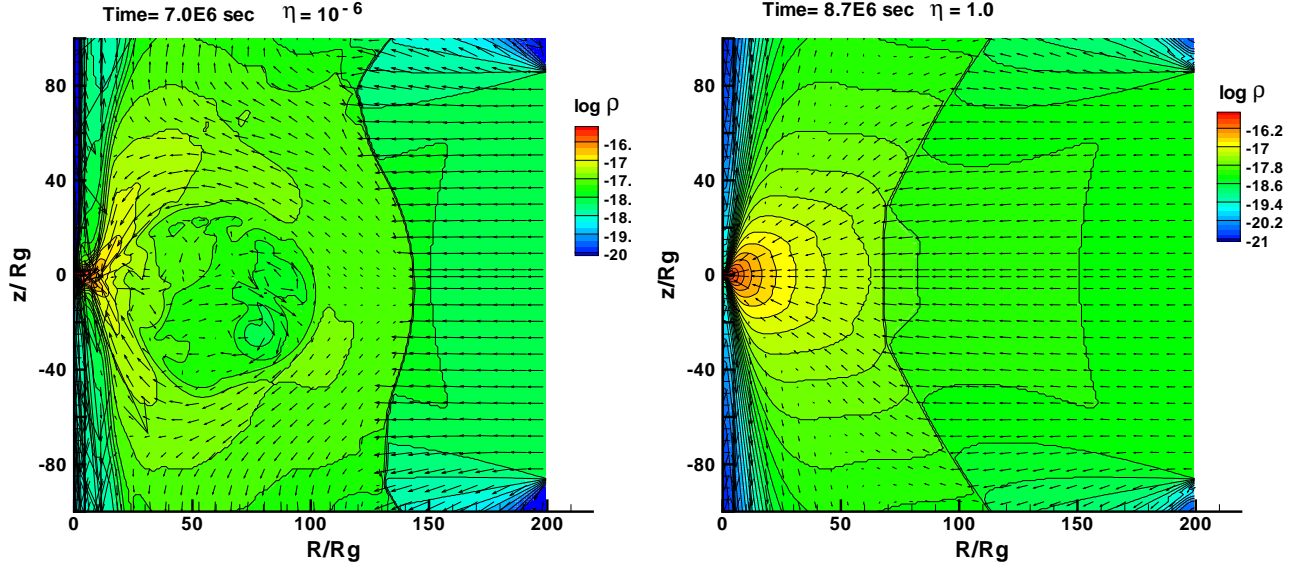
Fig. 8 2D density contours and velocity vectors of flows with $\eta = 10^{-6}$ and 1.0 at times $t = 7 \times 10^6$ and 8.7×10^6 s, respectively. In the former, variables of density and temperature are asymmetric with respect to the equator and turbulent motions are observed within the post-shock region but in the latter case the flow is almost symmetric with respect to the equator, and no turbulent motion appears. The shock locations are signified by *thick black contour lines*.

return to the initial hydrodynamical steady-state but with a bit larger shock location $R_s \sim 70R_g$ than $R_s \sim 65R_g$ in Figure 2, because magnetic pressure contributes to the pressure balance to some extent in the shock location.

4.3 Astrophysical Significance

The present results for cases with low resistivity of $\eta = 10^{-6}$ and 0.01 are very similar to those for the previous magnetized flow without resistivity (Okuda et al. 2019). Adopting the same parameters of the flow and magnetic field as the present study, they found that the centrifugally supported shock moves back and forth between $60\,R_g \leq R \leq 170R_g$ and that another inner weak shock appears irregularly with rapid variations due to the interaction of the expanding high magnetic blob with the accreting matter below the outer shock. The process repeats irregularly with an approximate time scale of $(4-5) \times 10^5$ s (~ 5 d) with an accompanying smaller amplitude modulation with a period of $\sim 0.9 \times 10^5$ s (25 hr). In this respect, we also analyzed the time variability of the resistive magnetized flows. Figure 9 shows the power density spectra of luminosity for different values of resistivity. For $\eta = 10^{-6}$ and 0.01, the peak (fundamental) frequency is estimated roughly to be at 2×10^{-6} along with two weak signatures (harmonics) at 7×10^{-6} and 2×10^{-5} Hz. These correspond to the periods of 5×10^5 s (5.8 d), 1.4×10^5 s (1.6 d) and 5×10^4 s (0.6 d), respectively

and are comparable to two QPO periods of ~ 5 d and ~ 1 d found in the non-resistive magnetized flow. Therefore the peak QPO frequencies can be associated with periods of ~ 5–10 d and ~ 1 d X-ray flares observed in the latest observations by Chandra, Swift and XMM-Newton monitoring of Sgr A* (Degenaar et al. 2013; Neilsen et al. 2013, 2015; Ponti et al. 2015). On the other hand, for $\eta = 0.1$ and 1.0, there is no clear peak frequency. The average mass outflow rate $\sim 10^{-6}\,M_\odot\,yr^{-1}$ and mass inflow rate $\sim 3 \times 10^{-6}\,M_\odot\,yr^{-1}$ obtained in small η cases affirm a roughly good correspondence with the Chandra observations (Wang et al. 2013) which suggests the presence of a high outflow rate that nearly balances the inflow rate.

5 SUMMARY

We studied the effect of resistivity on a standing shock in the magnetized flow around a black hole. The flow parameters of specific energy, $\epsilon = 1.98 \times 10^{-6}$, and specific angular momentum, $\lambda = 1.35$, with $\Gamma = 1.6$ have been considered to address the flow behavior around Sgr A*. For flows with lower resistivity $\eta = 10^{-6}$ and 0.01, the luminosity and shock location on the equator vary quasi-periodically. These QPOs are attributed to the interactive result between the outer oscillating standing shock and the inner weak shocks occurring at the innermost hot blob. The luminosity varies maximumly by a factor of
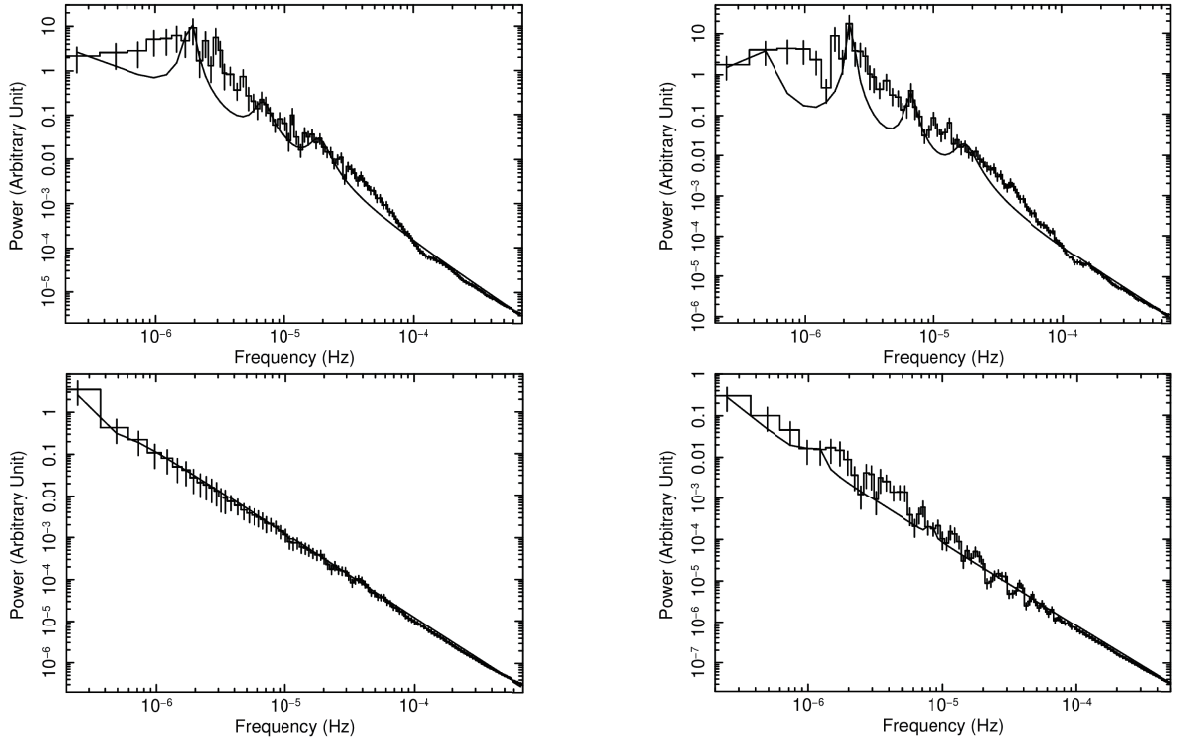
Fig. 9 Power density spectra for a resistive MHD flow with different resistivity values $\eta = 10^{-6}$, 0.01, 0.1 and 1 (in the clockwise direction).

ten around the average $L \sim 3.0 \times 10^{34}$ erg s^{-1}. The mass outflow rate is very large at a few tens of percent of the input accretion rate. The MHD turbulence seems to play important roles in the outward transport of not only angular momentum but also accreting gas. The power density spectra of luminosity variation exhibit the peak frequencies which correspond to the periods of 5×10^5 s (5.8 d), 1.4×10^5 s (1.6 d) and 5×10^4 s (0.6 d). While for cases with higher resistivity of $\eta = 0.1$ and 1.0, the flow becomes steady and symmetric with respect to the equator. Variable features of the luminosity disappear here and a steady standing shock is formed more outward compared with the hydrodynamical flow. The mass outflow rate is also as high as $\sim$ a few tens of % of the input gas. The high resistivity considerably suppresses the magnetic activity such as the MHD turbulence and tends to make the magnetized flow be stable and symmetric with respect to the equator. The low angular momentum magnetized flow model with low resistivity is a possible explanation for the high mass outflow rate of $\sim 10\%$ of the Bondi accretion rate $\sim 1 \times 10^{-5}$ $M_\odot \mathrm{yr}^{-1}$ as suggested by Chandra observations (Wang et al. 2013) and of the long-term flares with $\sim$ one per day and $\sim$ 5–10 days of Sgr A* in the latest observations by Chandra, Swift and XMM-Newton monitoring of Sgr A*.

References

Aktar, R., Das, S., & Nandi, A. 2015, MNRAS, 453, 3414

Balbus, S. A., & Hawley, J. F. 1998, Rev. Mod. Phys, 70, 1

Becker, P. A., Das, S., & Le, T. 2008, ApJ, 677, L93

Bondi, H. 1952, MNRAS, 112, 195

Chakrabarti, S. K. 1989, ApJ, 347, 365

Chakrabarti, S. K. 1993, MNRAS, 261, 625

Chakrabarti, S. K. 1996, ApJ, 464, 664

Chakrabarti, S. K., Acharyya, K., & Molteni, D. 2004, A&A, 421, 1

Chakrabarti, S. K., & Molteni, D. 1993, ApJ, 417, 671

Chakrabarti, S. K., & Molteni, D. 1995, MNRAS, 272, 80

Chakrabarti, S. K., Mondal, S., & Debnath, D. 2015, MNRAS, 452, 3451

Chakrabarti, S. K., & Titarchuk, L. 1995, ApJ, 455, 623

Chattopadhyay, I., & Kumar, R. 2016, MNRAS, 459, 3792

Das, S., Chattopadhyay, I., Nandi, A., & Chakrabarti, S. K. 2001, A&A, 379, 683

Das, S., Chattopadhyay, I., Nandi, A., & Molteni, D. 2014, MNRAS, 442, 251

Das, T. K., Nag, S., Hegde, S., et al. 2015, New Astronomy, 37, 81

Degenaar, N., Miller, J. M., Kennea, J., et al. 2013, ApJ, 769, 155

Fukue, J. 1987, PASJ, 39, 309

Fukumura, K., Takahashi, M., & Tsuruta, S., 2007, ApJ, 657, 415

Giri, K., & Chakrabarti, S. K. 2013, MNRAS, 430, 2836

Giri, K., Garain, S. K., & Chakrabarti, S. K. 2013, MNRAS, 448, 3221

Gu, W. M., & Foglizzo, T. 2003, A&A, 409, 1

Gu, W. M., & Lu, J. F. 2006, MNRAS, 365, 647

Hawley, J. F., & Balbus, S. A. 1991, ApJ, 376, 223

Kim, J., Garain, S. K., Balsara, D. W., & Chakrabarti, S. K. 2017, MNRAS, 472, 542

Kim, J., Garain, S. K., Chakrabarti, S. K., & Balsara, D. S., 2019, MNRAS, 482, 3636

Kumar, R., & Chattopadhyay, I. 2013, MNRAS, 430, 386

Kumar, R., & Chattopadhyay, I. 2014, MNRAS, 443, 3444

Lanzafame, G., Cassaro, P., Schilliró, F., et al. 2008, A&A, 482, 473

Lanzafame, G., Molteni, D., & Chakrabarti, S. 1998, MNRAS, 299, 799

Le, T., Wood, K. S., Wolff, M. T., et al. 2016, ApJ, 819, 112

Lee, S.-J., Ryu, D., & Chattopadhyay, I. 2011, ApJ, 728, 142

Lee, S.-J., Chattopadhyay, I., Kumar, R., et al. 2016, ApJ, 831, 33

Liang, E. P. T., & Thompson, K. A. 1980, ApJ, 240, 271L

Lu, J. F., Gu, W.-M., & Yuan, F. 1999, ApJ, 523, 340

Mandal, S., & Chakrabarti, S. K. 2010, ApJ, 710, L147

McKinney, J. C., & Gammie, C. F. 2002, ApJ, 573, 728

Michel, F. C. 1972, AP&SS, 15, 153

Mignone, A., Bodo, G., Massaglia, S., et al. 2007, ApJS, 170, 228

Mignone, A., Zanni, C., Tzeferacos, P., et al. 2012, ApJS, 198, 7

Molteni, D., Lanzafame, G., & Chakrabarti, S. K. 1994, ApJ, 425, 161

Molteni, D., Lanzafame, G., & Chakrabarti, S. K. 1996, ApJ, 470, 460

Molteni, D., Sponholz, H., Chakrabarti, S. K. 1996, ApJ, 457, 805

Molteni, D., Toth, G., & Kuznetsov, O. A. 1999, ApJ, 516, 411

Moscibrodzka, M, Das, T. K., & Czerny, B. 2006, MNRAS, 370, 219

Nakayama, K. 1992, MNRAS, 259, 259

Nakayama, K. 1992, MNRAS, 270, 871

Narayan, R., Kato, S., & Honma, F. 1997, ApJ, 476, 49

Narayanm, R., & Yi, I. 1994, ApJ, 428, L13

Neilsen, J., et al. 2013, ApJ, 774, 42

Neilsen, J., et al. 2015, ApJ, 799, 199

Nobuta, K., & Hanawa, T. 1994, PASJ, 46, 257

Novikov, I. D., & Throne, K. S. 1973, in Black Holes, eds. B. S. Dewitt, & C. Dewitt (New York: Gordon and Breach) 343

Okuda, T., Singh, C. B., Das, S., et al. 2019, PASJ, 71, 49

Okuda, T., Teresi, V., & Molteni, D. 2007, MNRAS, 377, 1431

Paczyńsky, B. & Wiita, P. J. 1980, A&A, 88, 23

Ponti, G., et al. 2015, MNRAS, 454, 1525

Proga, D., & Begelman, M. C. 2003, ApJ, 592, 767

Roy, A., & Chakrabarti, S. K. 2017, MNRAS, 472, 4689

Ryu, D., Chakrabarti ,S. K., & Molteni, D. 1997, ApJ, 474, 378

Shakura, N. L., & Sunyaev, R. A. 1973, A&A, 24, 337

Singh, C. B., & Chakrabarti, S. K. 2011, MNRAS, 410, 2414

Smith, D. M., Heindl, W. A., Markwardt, C. B., & Swank, J. H. 2001, ApJ, 554, 41

Smith, D. M., Heindl, W. A., & Swank, J. H. 2002, ApJ, 569, 362

Stone, J. M., & Pringle, J. E. 2001, MNRAS, 322, 461

Takahashi, M., Goto, J., Fukumura, K., et al. 2006, ApJ, 645, 1408

Wang, Q. D., Nowak, M. A., Markoff, S. B., et al. 2013, Science, 341, 981